LA-UR- 11-01963

Approved for public release; distribution is unlimited.

Title:	Research Overview and Proposal
Author(s):	Moro, Erik A., INST-OFF, eamoro@lanl.gov
Intended for:	Intended for presentation at a technical meeting on April 18th, 2011, at the UCSD campus in La Jolla, CA, USA, regarding a joint UCSD/LANL research project.

Los Alamos
NATIONAL LABORATORY
EST. 1943

Form 836 (7/06)

Research Overview and Proposal

Erik A. Moro, Ph.D. Student UCSD Department of Structural Engineering, eamoro@lanl.gov
Advisor: Prof. Michael D. Todd, UCSD Department of Structural Engineering, mdt@ucsd.edu

ABSTRACT

A variety of intensity-modulated optical displacement sensor architectures have been proposed for use in non-contacting sensing applications; with one of the most popular being the bundled displacement sensor. Of the bundled displacement sensors that have been reported, it does not appear that anyone has used a validated model of the transmission from a single mode optical fiber to accurately simulate the sensor's performance *a priori* or guide the design of the bundle arrangement. The radial intensity distribution of a transmission from a single mode optical fiber is often approximated using Gaussian-shaped spatial field distributions, and while such approximations are useful for some applications, they do not accurately describe optical transmission intensity off of the axis of propagation. A recent paper was presented that more accurately describes the intensity distribution, and this document describes a simple experimental setup that was performed to verify the model's accuracy through formal uncertainty quantification procedures; establishing agreement between model and experiment both on and off of the axis of propagation. These results are then discussed in the context of displacement sensor designs based on the optical lever architecture. Transmission behavior off of the axis of propagation controls the sensor performance when large lateral offsets (25-1500 μm) exist between transmitting and receiving fibers. The practical implications of modeling accuracy at large lateral offsets are discussed as they relate to the development of high-performance, intensity-modulated optical displacement sensors. Specifically, the sensitivity, linearity, resolution, and displacement range of a sensor are functions of the relative positioning of the sensor's transmitting and receiving fibers. In this document the validated transmission model is used to describe the bundle sensor design space, and an optimization approach that employs a genetic algorithm efficiently explores this design space. From the converged output of a genetic algorithm a high-sensitivity bundled displacement sensor configuration that offers linear performance is simulated, with sensitivity of 0.050 μm^{-1} and a maximum absolute output error of 3.0 over the axial displacement range of 6-8 mm. This optimized bundle configuration is manufactured and tested experimentally, with a sensitivity of 0.052 μm^{-1} and a maximum absolute output error of 8.3 over the axial displacement range of 6-8 mm.

This approach may be generalized to determine an optimized bundle configuration that offers high-sensitivity performance for a variety of axial displacement ranges. Proposed continuations of this research include the extension of this optimization approach as a generalized sensor design tool that describes intensity-modulated optical displacement sensor performance characteristics in terms of the sources of modeling and experimental uncertainty that are present. Another proposed continuation of this research is the application of these validation and uncertainty analysis principles for use in the characterization of non-contacting interferometric optical displacement sensors. These two thrusts will equip one to make side-by-side comparisons of the two displacement sensing methodologies in terms of desired performance metrics as they relate to unavoidable sources of uncertainty.

1. INTRODUCTION

In certain sensing applications, fiber optic sensors offer the advantages over traditional electro-mechanical sensors of being both immune to electromagnetic interference and non-spark emitting [1], and because of the low levels of opto-electrical noise, they offer the potential for increased resolution [1]-[3]. Non-contacting fiber optic sensors have also been proposed for kinematic sensing applications that require minimal invasiveness [3]. The primary objective of this research is to design a non-contacting, optical displacement sensor that modulates displacement linearly as a simple (e.g., voltage) output with minimal signal processing. A secondary goal of this research is that such a sensor exploits high-performance architectures that exist within the sensor design space. The goal of high-performance necessitates an investigation of the fundamental relationships between sensor parameters, signal demodulation techniques, and performance metrics within a particular set of design constraints and requirements. These goals depend on the accurate calculation of the sensor design space.

2. MOTIVATION FOR INTENSITY-MODULATED SENSING

The implementation of fiber optic sensors has become increasingly widespread in the last few decades, as hardware has been developed and been made less expensive [1]-[3]. The most popular types of non-contacting, fiber optic

displacement sensors are the extrinsic Fabry-Perót interferometric (EFPI) displacement sensor [4]-[5] and variations on the optical-lever-style intensity-modulated displacement sensor [6]-[8]. In an EFPI displacement sensor, the source's transmission is separated into two components that interfere with one another, and displacement is modulated as a function of phase changes in the interference pattern that forms when they are recombined [4]. Typical EFPI sources transmit in either the ultraviolet, visible, near-infrared, or short-wavelength infrared ranges. As a result of the small scale of the transmission's wavelength (less than 2 μm), these phase changes are highly-sensitive to changes in displacement, creating the possibility for high-accuracy EFPI displacement sensors. This performance advantage, however, comes at a cost, since the signal processing required to demodulate displacement from phase currently restricts the sensor's bandwidth to the low-kHz range. The accuracy and bandwidth of a particular EFPI displacement sensor are largely governed by the specific signal processing techniques that are implemented to demodulate phase. Since phase-demodulation is independent of the average measured power level, an additional advantage lies in the fact that even the simplest EFPI displacement sensors are robust to various fluctuations in measured power level that are not the result of changes in target displacement (e.g., fluctuations in source power level, optical loss mechanisms, surface reflectivity, etc...).

The simplest intensity-modulated optical displacement sensor architecture, referred to as the optical-lever, was originally independently proposed by Frank in 1966 [6] and Kissinger in 1967 [7] (Figure 1). Generally speaking, intensity-modulated displacement sensors exploit the relationship between target displacement and the measured power level of the electromagnetic transmission, which reflects off the target surface and is detected at one or more fixed locations. Although a displacement sensor based on the intensity-modulated optical-lever is inherently less sensitive to changes in displacement than the phase-modulated EFPI displacement sensor, the intensity-modulated approach offers the advantage that only the simplest computation is required to demodulate target displacement from measured optical power levels. As a result, large sampling rates, which are limited only by the bandwidths of the photodetector and the data acquisition hardware (on the order of hundreds of kHz through GHz), may be achieved.

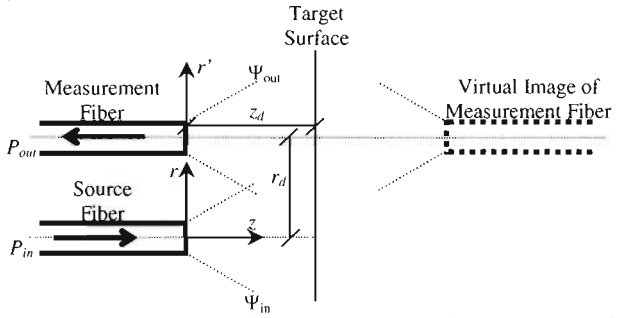

Figure 1. The simple, optical lever architecture is shown in relation to the coordinates introduced in Section 4. The virtual image relationship is exploited in the experimental setup (Section 5).

The primary drawback associated with intensity-modulated displacement sensors is that the reflected and measured power level at a single location is not robust to the previously mentioned environmental and hardware fluctuations. In other words, changes in the measured power level may not necessarily indicate changes in target displacement. This undesirable characteristic has motivated the research of robust, differential intensity-modulated sensors that make use of power measurements at multiple locations, examples of which were reported in 1999 [9] and 2004 [10]. A general representation of a differential sensing architecture is shown in Figure 2. By taking the ratio of two measured power levels, collected over an arbitrary spatial range, fluctuations in the transmission power level that occur prior to emission from the transmitting fiber are eliminated from the final measurement. Various differential intensity-modulated sensor architectures have been proposed; all of which employ just a few receiving fibers [9]-[12]. However, the relationship between the locations of the receiving fibers in these proposed sensors and sensor performance has not been thoroughly investigated.

Bundled intensity-modulated sensor architectures offer inherent performance advantages over architectures that contain only a few receiving fibers by measuring a greater portion of the reflected light and thereby exhibiting greater sensitivity to changes in target displacement (Figure 2). Bundled intensity-modulated displacement sensors were first implemented in research in 1979 [8] and have been implemented more recently with various design perturbations in 1996 [11] and in 2008 [12]. They are also currently commercially available [13]-[14]. Although bundled architectures have been a topic of research since 1979; little if any consideration has been given to the possibility of combining the increased performance of the bundled architecture with the robustness of the differential

approach. Further, to the best of the author's knowledge, the relationship between fiber location and sensor performance has not been used to guide the design of intensity-modulated optical displacement sensors with application-specific, high-performance combinations of resolution, sensitivity, and axial displacement range. The author has shown the existence of multiple regions of linear sensitivity for various relative positions of transmitting and receiving fibers within a two-fiber optical lever [15], with the different regions exhibiting different combinations of linear sensitivity and axial displacement range. The implication is that the bundled architecture's design space could contain optimal combinations of linear sensitivity and axial displacement range that meet the performance needs of a given sensing application. By extension, a bundled intensity-modulated displacement sensor may be designed, as shown in Figure 2, with multiple groups of receiving fibers, such that high-performance and robust differential demodulation are both achieved.

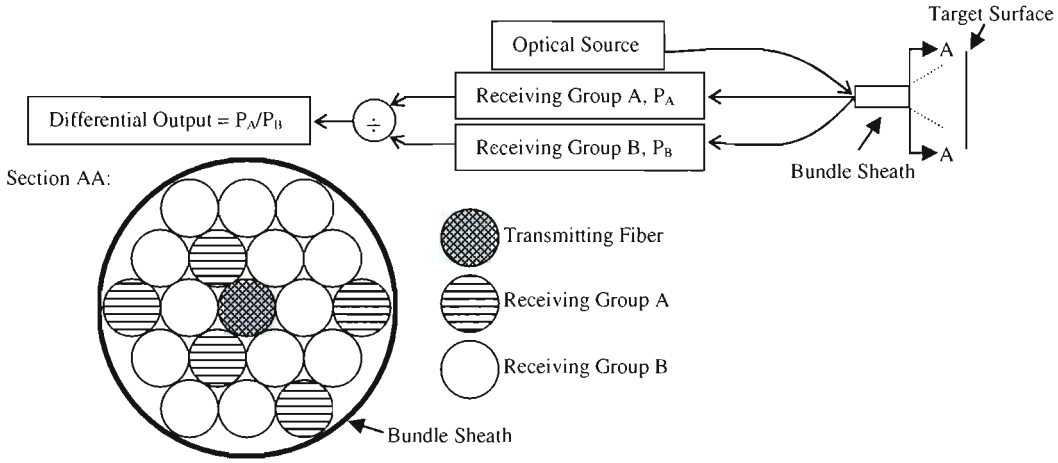

Figure 2. The bundled differential approach offers the potential for robust, high-performance non-contact optical displacement sensing.

3. PREVIOUS IMPLEMENTATIONS OF INTENSITY-MODULATED SENSORS

Perhaps the primary reason that the relationship between fiber location within a bundled architecture and sensor performance has not yet been used to guide sensor design is that the most widely implemented models used to simulate optical transmission behavior suffer from significant inaccuracies. Initially, the performance of the optical-lever architecture was simulated using a ray-optic model; relating bundle geometry to experimentally measured optical power levels [8], [9]-[11]. This model demanded little computation and generally captured the divergence behavior of a transmission propagating through space. However, implicit in this model is the assumption that the illumination is uniform, and therefore this model has no utility in describing the intensity distribution of a propagating transmission. Recently, more sophisticated models that approximate the radial intensity distribution using a Gaussian function have been proposed [12]. These approximations have been widely implemented, are relatively simple to compute, and are more accurate than the ray-optic models in describing the intensity-distribution of the LP_{01} mode, the only mode that propagates within a single mode optical fiber [16]. However, the accuracy of Gaussian approximations decreases off the axis of propagation, limiting their usefulness to conceptual visualization, component alignment, and the rough approximation of off-axis power levels. Consider the hexagonal close-packed bundle architecture shown in Figure 2; where the cores of adjacent fibers are separated by at least the diameter of the fiber coating (250 μm is typical). This radial offset between cores is large enough to render the Gaussian approximation useless in determining the measured power levels at any of the receiving fibers without large uncertainty. Therefore, if a model is intended for the accurate characterization of the bundle architecture design space, the Gaussian model has insufficient accuracy to be seriously considered.

4. PHYSICS-BASED TRANSMISSION MODEL

A model that accurately characterizes measured optical power levels off the transmission's axis of propagation was derived from the physics of electromagnetic wave propagation subject to the boundary conditions imposed by a step-index single mode optical fiber by Trudel and St-Amant in 2009 [17]. Although Trudel and St-Amant did an excellent job introducing the physics-based model and qualitatively discussing its performance, they did not address in any capacity model verification or uncertainty analysis, nor did they include a quantitative description of the error between the model and the reported experimental results. This document describes work that the author has

performed in an effort to verify the performance of and analyze the effects of uncertainty on this physics-based model [18]. This document also describes the manner in which this model, once verified, may be implemented for exploiting a large design space of bundled sensor architectures, in an attempt to achieve high-performance while meeting application-specific performance requirements. The fundamental LP_{01} mode, the only mode that propagates within a single mode optical fiber, has a field function that is given by

$$\Psi(r)=\begin{cases}\Psi_0 J_0\left(\dfrac{ur}{a}\right) & r<a\\ \Psi_0\dfrac{J_0(u)}{K_0(w)}K_0\left(\dfrac{wr}{a}\right) & r\geq a.\end{cases} \qquad (1)$$

Ψ_0 is the field magnitude, a is the diameter of the optical fiber core, J_0 and K_0 are the order-zero Bessel functions of the first and second kind, respectively, u is the normalized transverse propagation constant, and w is the normalized transverse attenuation constant. The propagating mode within the transmitting optical fiber ultimately exits the fiber tip where it diffracts into the surrounding air (Figure 1). After emitting through the tip of the transmitting fiber, the fundamental mode propagating through the air $\Psi_{out}(r,\theta,z)$ may be expressed as

$$\Psi_{out}(r,\theta,z)=\left(\frac{2j\pi}{\lambda z}\right)\int_0^\infty r'\exp\left(\frac{-j\pi}{\lambda z}\left(r'^2+r^2\right)\right)J_0\left(\frac{2\pi rr'}{\lambda z}\right)\Psi(r')dr'. \qquad (2)$$

Equation (2) is taken from the formulation for a cylindrically symmetric mode diffracting through a circular aperture [19]. In this formulation, the field $\Psi(r')$ propagates within the receiving optical fiber and the output field $\Psi_{out}(r,\theta,z)$ is the acceptance field of the receiving fiber. λ is the wavelength of the propagating light, $j=\sqrt{-1}$, (r,θ) are the coordinates of the input (transmitting fiber) frame, and (r',θ') are the coordinates of the output (receiving fiber) frame. The input and output coordinate frames are related by

$$r^2=r'^2+r_d^2+2r'r_d\cos(\theta'-\theta_d). \qquad (3)$$

r_d and θ_d constitute the translation and rotation between frames (Figure 1). For the purposes of this work, θ_d is always assumed to be zero, and r_d is referred to as the lateral offset between the transmitting and a given receiving fiber. The coupling efficiency between the two fibers, or the fraction of the transmitted light that enters the receiving fiber, may be calculated using the normalized overlap integral [20], expressed in cylindrical coordinates as

$$\eta(r_d,z)=\frac{P_{out}}{P_{in}}=\frac{\left|\int_0^{2\pi}\int_0^\infty r\Psi_{in}\Psi_{out}^*\,dr\,d\theta\right|^2}{\left|\int_0^{2\pi}\int_0^\infty r\Psi_{in}\Psi_{in}^*\,dr\,d\theta\int_0^{2\pi}\int_0^\infty r\Psi_{out}\Psi_{out}^*\,dr\,d\theta\right|} \qquad (4)$$

where, $\Psi_{in}=\Psi(r)$ as given in (1), and $\Psi_{out}=\Psi_{out}(r,\theta,z)$ as given in (2). By evaluating (4), the measured optical power at any point in space may be calculated, given a particular set of transmitting and receiving field functions. Rational bounds need to be chosen for the limits of integration over the radial coordinate r in both the overlap integral (4) and the diffraction integral (2). After running numerous simulations, appropriate limits were established that differ significantly from the original values reported in [17]. For the level of numerical precision used during computation, an upper limit of r'=20 μm was sufficient for the calculation of (2) at all of the axial displacements explored over the range 1000 μm to 50 000 μm. For the same level of precision, the upper limits on (4) ranged from r=400 μm at an axial displacement of 1000 μm to r=3900 μm at an axial displacement of 50 000 μm.

5. TEST-BENCH EXPERIMENTAL SETUP

The experimental setup that was used to verify the accuracy of the model presented in Section 4 is shown in Figure 3. Optical power was sampled as a function of the relative position between the transmitting and receiving fibers by positioning the receiving fiber at a given axial displacement $z=z_d$ and scanning across a range of lateral offsets r_d (3), in order to verify the accuracy of the model described in Section 4.

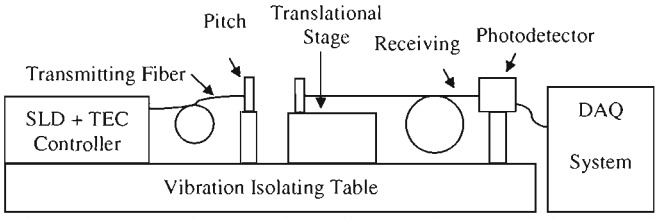

Figure 3. The test-bench experimental setup, used for experimentally measuring transmission power levels as a function of radial offset and axial displacement, is shown here.

The optical source used for this experiment was a 5 mW super luminescent diode (SLD), centered at 1528 nm, which was controlled with a laser driver/thermoelectric cooler. Single mode step index optical fibers, a broadband InGaAs photodetector centered at approximately 1550 nm, and a data acquisition module with an impedance of 1 MΩ were used for reading the power level at the receiving fiber tip. A 3-axis translational stage and a 1-axis translational stage were used for precise control of the receiving fiber position. The transmitting fiber was mounted on a device with pitch control so that alignment with the receiving fiber could be established.

During experimental testing, z_d was varied from 1000 μm to 50 000 μm. For larger axial displacements, the SLD's maximum rated output power of 5 mW was used in order to minimize the effects of quantization error. For smaller axial displacements, a lower output power was used to avoid saturation of the photodetector. In all cases the results were normalized by the transmitted power level, which was provided by the manufacturer as a function of input current and independently experimentally verified during testing. At a given $z=z_d$, r_d was incrementally increased by a fixed amount, creating a lateral offset to one side of the transmitting fiber. The mean of 1000 photodetector power readings, sampled at 1 kHz, was calculated at each position. When the signal became sufficiently weak (between -50 dBm and -60 dBm), r_d was decreased and re-sampled at the same points, bringing the receiving fiber back to zero lateral offset. This procedure resulted in two samples at each point in space. Next, the same procedure was carried out in the other direction, creating a lateral offset to the other side of the transmitting fiber. Once again, these points were each sampled twice, once while increasing the offset and once while decreasing the offset. Scanning on both sides of the transmitting fiber tip was performed to ensure symmetry in the transmission's power distribution, which is a good indication of alignment between the transmitting and receiving optical fibers. These scans resulted in a partial view of the power distribution of the transmitted signal, a subset of which are shown in Section 6.4.

The noise floor of the test setup was estimated by using the data acquisition module to measure the photodetector's output while no transmitting signal was being sent by the SLD. As in the case of the previously described transverse scans, each power measurement was calculated as the mean of 1000 photodetector measurements sampled at 1 kHz. The mean of the noise data was the same if the photodetector was disconnected from the data acquisition module, suggesting that the observed noise floor is that of the data acquisition module. During testing, the noise floor was between -60 dBm and -50 dBm depending on the source power level (since experimental results were normalized by the source power level). The mean and variance of these noise samples were calculated so that the effect of the noise floor could be reproduced in the simulation results.

6. MODEL VERIFICATION AND UNCERTAINTY QUANTIFICATION

6.1 Experimental Uncertainty

For the test-bench described in Section 5, experimental uncertainty results from a lack of knowledge regarding the initial distance calibration between fiber tips, the true changes in fiber tip position (limited by micrometer resolution), and optical loss mechanisms, and from random behavior in the optical source, photodetector, and data acquisition system. These sources of uncertainty may be analyzed in an effort to better understand the impact they have on the measured power level (the simulation output) and the corresponding implications on sensor design. The bias error that results from distance calibration is assumed to be less than ±10 μm. Using a first-order approximation, this error can be converted to units of dB by the derivative of the received power with respect to axial displacement, which itself is a function of axial position (Figure 4). Specifically, at a radial offset of 250 μm a bias measurement error of 0.1 dB would result from a 10 μm bias at an axial displacement of 1000 μm, but the bias would be less than 0.01 dB assuming the same radial offset at an axial displacement of 50 000 μm. The implication is that during testing the true axial displacement may have been offset from the estimated axial displacement by a constant value of as much as 10 μm, resulting in a bias error of as much as ±0.1 dB in the measured power level.

User error during the transverse scanning process may result in a position discrepancy of up to ± 2.5 μm, which is the resolution of the micrometers employed. Implementing the same first-order sensitivity approach discussed in the previous paragraph and replacing axial sensitivities with transverse sensitivities, 2.5 μm corresponds to 1.0 dB at a radial offset of 250 μm and an axial distance of 1000 μm, and less than 0.01 dB at a radial offset of 250 μm and an axial distance of 50 000 μm. The implication is that during testing, the lateral difference between the actual receiving fiber position and the assumed receiving fiber position could have been as much as ± 2.5 μm, which would have resulted in a resolution error of up to ± 1.0 dB in the measured power level.

Random noise on the SLD output, the photodetector, and the data acquisition system were measured, resulting in a combined deviation of ± 0.015 dB from the mean power level at a given point in time. Additionally, the effects of long-term drift in the source power level (measured over 24 hours) were found to be less than 0.2 dB. Therefore the combined effects of these uncertainties on the measured power level are estimated to be as much as 0.215 dB. The estimated effects of this and the previously described sources of experimental uncertainty are summarized in Table I. The primary loss mechanisms in the test-bench experimental setup were polarization dependent loss (PDL) and coupler insertion losses. The rotation of the coiled optical fibers in the experimental setup was adjusted until it was concluded that PDL had been approximately minimized. According to component manufacturers, the total insertion loss in the experimental setup can be estimated as less than 0.65 dB. Assuming zero PDL, these loss mechanisms result in a wavelength-independent offset between experimental results and simulation results of less than 0.65 dB.

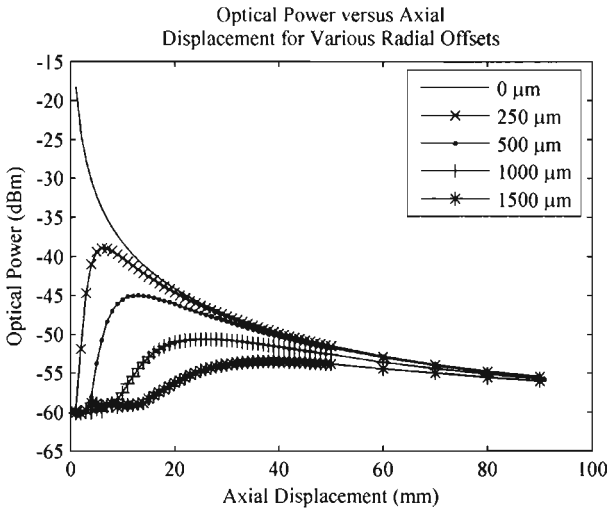

Figure 4. Experimentally measured power is plotted as a function of axial displacement at a radial offsets ranging from 250 μm to 1500 μm. The slope represents the change in power divided by the change in axial displacement, which itself changes as a function of both radial offset and axial displacement.

6.2 Modeling Uncertainty

Modeling uncertainty results from a lack of knowledge regarding the model's input parameters. Although no numerical approximation is perfectly accurate, it was assumed for this work that truncation errors resulting from finite computational precision are not significant compared to the effects of input parameter uncertainty. The input parameters in (1)-(4) include a, λ, u, and w, in addition to E_0, r, r_d, and z. Note that the uncertainty on E_0 and the uncertainty on the spatial coordinates r, r_d, and z were described the previous subsection.

A phenomenon identification ranking table (PIRT) may be used as a preliminary means of qualitatively assessing the significance of a particular parameter's uncertainty from the degree of the variability in that model input parameter and the sensitivity of the model output to that variability [21]. The results of a PIRT analysis for this application showed that variability in λ is expected to have a relatively small effect on the simulation output, while variability in a, n_1, and n_2 has the potential to significantly impact the simulation output. The value of and the tolerances on a are both specified by the fiber manufacturer, but assumptions have to be made regarding the nature and the magnitude of the uncertainty on n_1 and n_2. Recall that the effects of experimental uncertainty were directly observed as fluctuations in the measured power level. However, since these sources of modeling uncertainty affect the simulation output indirectly, the full ranges of possible values for uncertain input parameters must be propagated

through the numerical model in order to see the corresponding range of possible output values. This process is discussed in detail in the following sub-section.

6.3 Effect Screening and Uncertainty Propagation

After performing the PIRT analysis, effect screening was performed for the purpose of reducing the number of input parameters required in the uncertainty propagation stage [22]. Parameter down-selection is critical when simulation trials are computationally expensive and a reduction in the complexity of the uncertainty propagation process therefore results in significant time and computational cost savings. For this paper, a three-level full factorial design of experiments was used to test the effects that variability in E_0, a, n_1, and n_2 has on the measured optical power level at various points in (r, z) space, requiring 3^4=81 trials. The design space explored for these input parameters is summarized in Table I. Note that probability density functions (PDFs) do not have to be assumed for these uncertain input parameters during the screening process [22]. Rather, these input parameters were sampled uniformly over the entire range of possible values in order to assess the total potential impact of their variability on the variability of the model's output. A four-way analysis of variance (ANOVA) performed between the four inputs (sampled over the design space) and the model's output provides insight into the impact each parameter's variability has on the variability of the model's output. R-squared values, calculated from the ANOVA, are shown in Figure 5, where a larger value indicates a stronger dependence between output variability and input parameter variability [22]. As can be seen from these results, variability fluctuations on E_0 and a have relatively negligible effect on output variability.

Table I. Experimental and Modeling Sources of Uncertainty

Source	Symbol	Nominal Value	Nominal Error	Error Range	Max. Impact	PDF
Tip Separation Distance	z	n/a	0 μm	±10 μm	1 dB	Unif.
Micrometer Resolution	r_d	n/a	0 μm	±2.5 μm	1 dB	Unif.
Opto-Electrical Noise/Drift	E_0	*n/a*	*0 dB*	*±0.215 dB*	*0.215 dB*	Gauss.
Core Radius	a	*4.1 μm*	*0 μm*	*±0.2 μm*	*n/a*	Unif.
Core Index of Refraction	n_1	1.4492	0	±0.0005	n/a	Gauss.
Cladding Index of Refraction	n_2	1.4440	0	±0.0005	n/a	Gauss.

The behavior of the sources of experimental and modeling uncertainty is summarized here. If applicable, the maximum estimated impact on the measured power level or the assumed probability distribution function is listed. The variability of parameters that are listed in italics were found during effect screening not to significantly impact output variability.

After effect screening, PDFs were assumed to describe the behavior of the uncertain input parameters (Table I). Simulations were run while using a Latin hypercube technique to sample r_d, z, n_1, and n_2 from their corresponding PDFs (listed in Table I). This resulted in a distribution of output (measured power) values at the sampled points in space. The results of this uncertainty propagation are overlaid on the results of the experimental scans in Section 5. Generally speaking, these results provide insight into the accuracy and the predictive capability of the model in the presence of well-described elements of uncertainty.

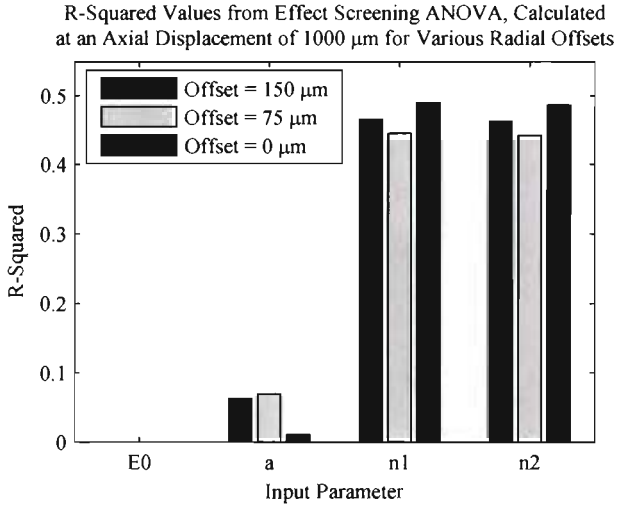

Figure 5. R-squared values, calculated from an ANOVA, are used to discriminate among those parameters whose variability significantly influences output variability and those whose influence is relatively insignificant.

6.4 Model Validation

Experimental results shown in Figure 6, illustrate the spatial behavior of the optical transmission. A close-up view of the transverse scan at an axial displacement of 1000 μm is shown in Figure 7. In these graphs, each experimental data point represents the average of two measurements taken at approximately the same point in space. The noise floor described in Section 5 and the 0.50 dB attenuation from the loss mechanisms described in Section 6.1 have been superimposed on the simulation results. Lines indicating the simulation results $\pm\sigma_{UP}$, one standard deviation calculated from the uncertainty propagated through the simulation, are shown to illustrate the level of agreement between experiment and simulation. As these results show, excellent agreement between the experimental results and the simulation results has been achieved, with most of the experimental measurements lying within $\pm\sigma_{UP}$ of the simulation results.

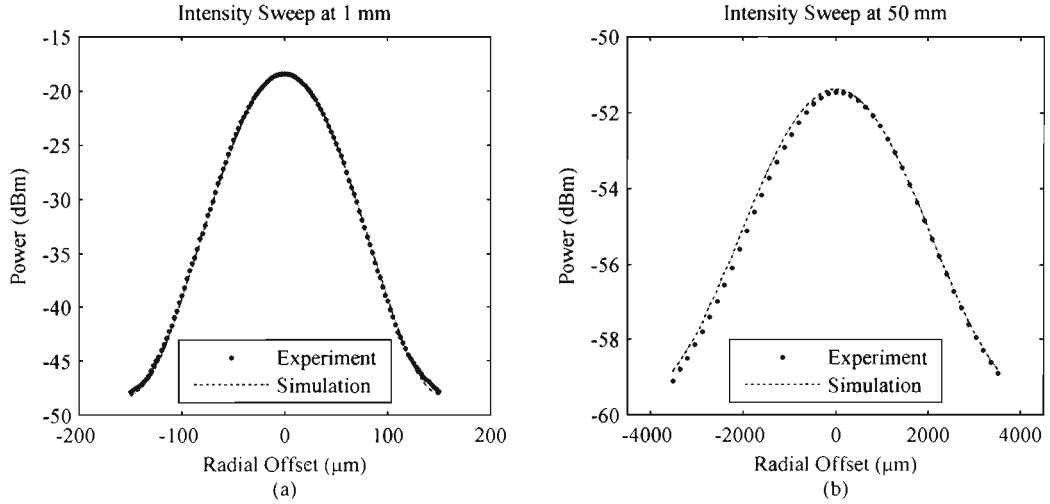

Figure 6. A comparison is shown between experimental and simulated power-distributions at axial displacements of (a) 1 mm and (b) 50 mm.

Given this formal validation, two trends are observed to accompany an increase in axial displacement. First, the overall power level diminishes. This is to be expected, as power is generally related to axial distance by an inverse-square relationship. Second, the modal field radius tends to increase as a result of divergence, causing the expected beam spreading of the transmission peak. These behaviors are captured well by the presented model. As expected, the power distribution is approximately Gaussian-shaped, which is the case for the LP_{01} mode. However, the agreement between the model and the experiment for large lateral offsets constitutes a noticeable improvement over

the use of Gaussian approximations. Note that not only is there good agreement describing peak magnitude and distribution shape, but also the power levels in the vicinity of the noise floor agree very well too, suggesting that the behavior of the observed noise floor, introduced in Section 5, is modeled accurately by the estimated noise floor.

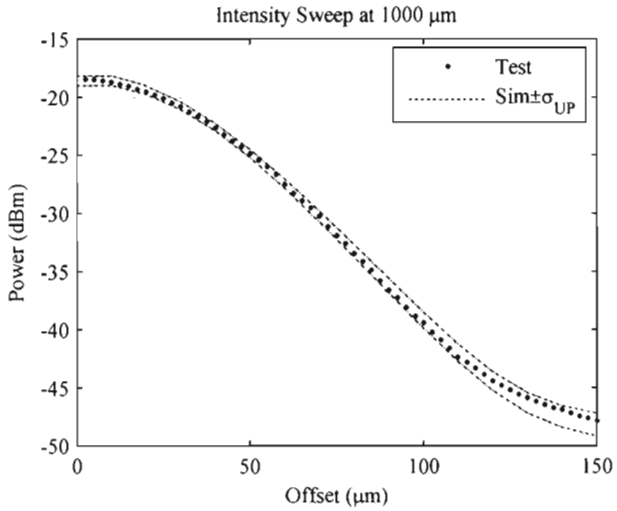

Figure 7. A close up view of Figure 6 (a) provides a useful visual comparison between simulation and experimental results. The experimental data points fit within the simulation results $\pm\sigma_{UP}$.

The root mean square error (RMSE) between the experimental results and simulated results is plotted at each experimentally tested axial displacement in Figure 8. This metric gives a clear representation of the absolute error between model and experiment for a given transverse scan, normalized by the number of points in that scan. The RMSE is observed to stay between 0.20 dB and 0.45 dB (Figure 8), which is on the order of the magnitude of σ_{UP}. While the agreement between the simulation results and the experimental results is strong, there is some error present with the received power as predicted by the simulation differing from the experimentally observed power level by as much as 0.1-1.0 dB at the tails of the transmission peak.

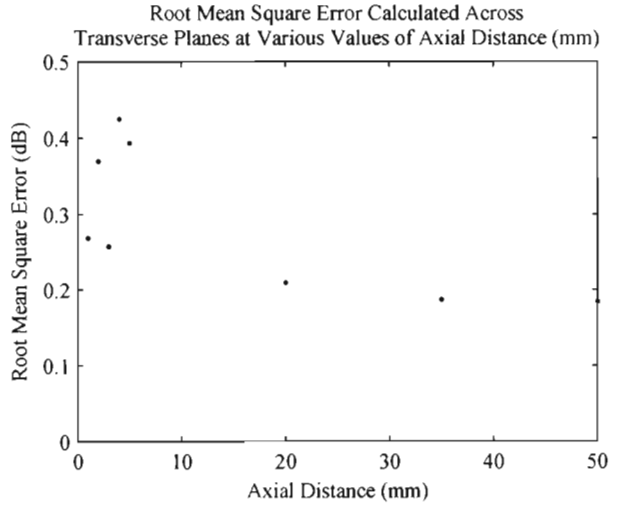

Figure 8. Root mean square error is calculated over a given transverse plane and plotted as a function of axial distance, providing insight into the discrepancy between simulation results and experimental results. The error is on the same order as σ_{UP}.

7. OPTIMIZED SENSOR PERFORMANCE

7.1 Simulation Results

A genetic algorithm was implemented to optimize the assignment of the receiving fibers are assigned to one of two, differentially interrogated receiving groups. The span of unique assignments of fibers to one of the two receiving

groups constitutes the optimization design space. It is assumed that each of the fibers belongs to one group or another, in the sense that each of the receiving fibers is employed for measurement. This is done in an effort to capture as much of the reflected light as is possible. In this paper, a sensor that offers highly-sensitive linear performance over an application-specific axial displacement range of 6-8 mm is specifically sought after. The approach used in this paper, however, may be generalized to other sensing applications by modifying the assumed operational displacement range, and the utility of this approach is that sensor configurations that exhibit relatively high combinations of sensitivity and linearity may be achieved over a spread of considered axial displacement ranges. The differential approaches described [9] and [10] were included in the implementation of the genetic algorithm, so both the ratio of one power level to another and the ratio of the difference of two power levels to their sum were considered, in addition to their reciprocals, resulting in a total of four differential approaches.

The converged output of the genetic algorithm illustrated that the optimized combination of sensitivity and linearity, over an axial displacement range of 6-8 mm, and with cost function weights of a=1 and b=4 (1), results from the bundle configuration shown in Figure 9. By using the ratio P_1/P_2 as a sensor output, the sensitivity of this differential sensor is -0.050 μm^{-1}, with a maximum absolute output error of 3.0, resulting in a displacement resolution of 60 μm, over an axial displacement range of 6-8 mm (Figure 10(a)). The separate numerator and denominator terms (P_1 and P_2, respectively) are shown in Figure 10(b). Intuitively this optimized result makes sense in that nearly the entire measured, received optical signal is grouped together, providing a relatively large power measurement P_1, and this large measurement is scaled by the relatively small P_2. Further, P_1 is the received power level calculated over most of the bundle tip and as a result it experiences averaging effects and is relatively constant over the entire 6-8 mm axial displacement range. P_2 changes, albeit slowly since it is measured at a large radial offset. These relationships are also detailed in Figure 10(b).

The optimization results varied depending on the differential sensing approach of interest, but the highest-sensitivity configuration was achieved when the ratio of P_1/P_2 was used as a sensor output (as shown in Figure 10(a) and (b)). Within the class of differential, non-contacting optical displacement sensors, an analogue sensitivity of 0.0322 μm^{-1} is reported with 99% linearity over an axial displacement range of about 75-125 μm [9], and to the best of the author's knowledge a higher-performing differential optical displacement sensor has yet to be reported. By comparison, the optimization results presented in this paper constitute a significant improvement, with an increase in sensitivity over a much larger axial displacement range.

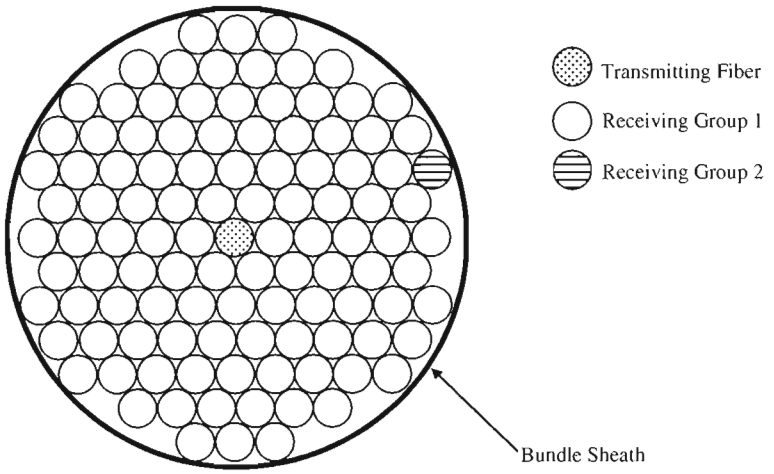

Figure 9. The bundle configuration output from the genetic algorithm is shown, with optimized performance being achieved when displacement is modulated as the ratio P_1/P_2.

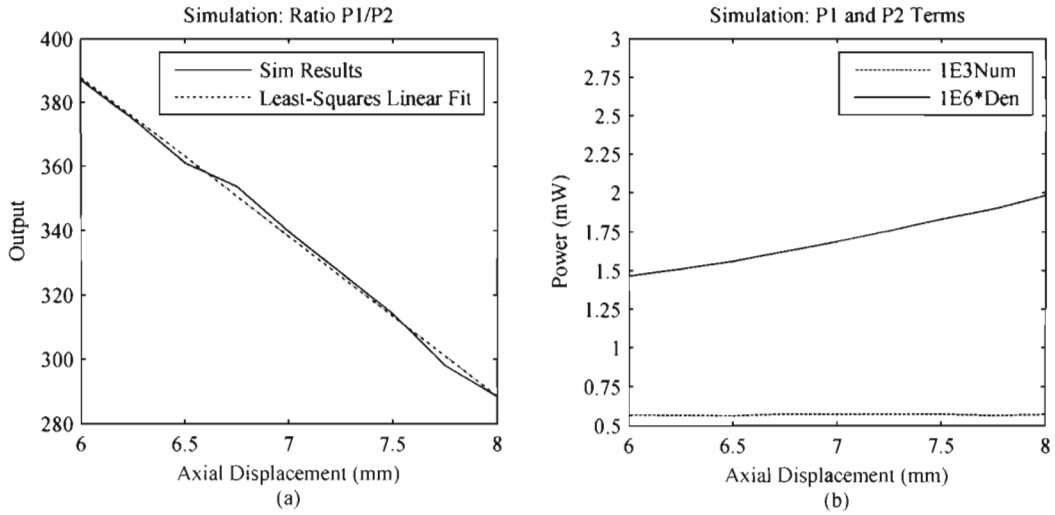

Figure 10. The output of the optimized sensor is shown as a function of axial displacement (a). The behavior of the numerator and denominator terms is shown as a function of axial displacement in (b).

7.2 Experimental Results

The bundle configuration specified by the output of the genetic algorithm was manufactured for the purpose of being experimentally tested, and the actual manufactured sensor, as bundled and grouped, is shown in Figure 11. Obviously the actual fiber bundling is not truly hexagonal close-packed, as was assumed during the implementation of the genetic algorithm (Figure 9), but a sufficient amount of the bundle is hexagonal close-packed that the simulation and optimization are still applicable. An appropriate fiber for use in Group 2 was determined (Figure 9) by selecting from a hexagonal close-packed sub-section of the bundle. Recall that Group 1 constitutes an averaged measurement over the majority of the bundle-face and that the measurement P_1 is approximately constant over the range of axial displacements from 6-8 mm (Figure 10 (a)). For these reasons, it is expected that the slight deviations in the actual manufactured bundle from a true hexagonal close-packed structure will have a negligible effect on the behavior of P_1, and by extension on the sensor output.

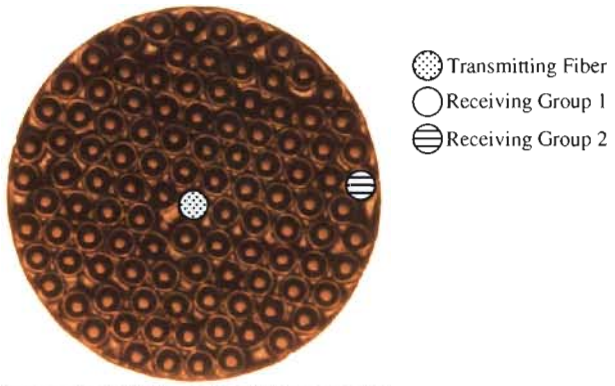

Figure 11. The actual bundle as manufactured and grouped differentiates slightly from the packing-structure that was assumed during optimization.

Please refer to the experimental setup shown in Figure 12. As stated previously, the optical fibers within the bundle were exclusively SMF-28e+ single mode step-index optical fibers. The target surfaces used were a front-surface protected silver coated mirror and a front-surface dielectric mirror with percent reflectivity at 1550 nm of about 98% and 25%, respectively. A pitch-control kinematic mount and a rotation platform were used to control the alignment of the bundle and the target surface, respectively. A 3-axis translational stage was used for positioning the sensor probe relative to the target surface. A 5 mW broadband super-luminescent diode centered at 1528 nm controlled by a thermoelectric cooler/controller acted as the optical source, and broadband photodetectors centered at 1550 nm and a data acquisition module were used for sampling and processing measurements of the received optical signal.

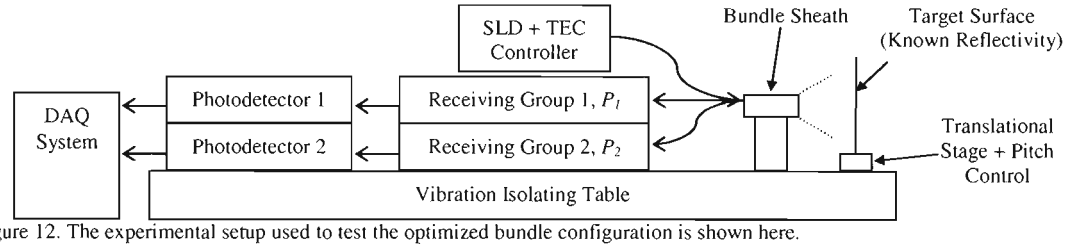

Figure 12. The experimental setup used to test the optimized bundle configuration is shown here.

The experimentally measured sensor output is shown in comparison to the simulated output of the optimized sensor configuration in Figure 13, with good agreement between simulation results and experimental results. The manufactured bundled displacement sensor is capable of measuring target displacement over a displacement range of 6-8 mm, with a sensitivity of -0.052 μm^{-1} and an absolute maximum output error of 8.3. This compares to the simulated sensor performance, which predicted operation over a range of 6-8 mm with a sensitivity of -0.050 μm^{-1} and an absolute maximum output error of 3.0. Sources of experimental and modeling uncertainty may very well be able to explain the increase in maximum output error in the experimental case. With this particular sensor, the resolution over the axial displacement range of 6-8 mm is limited by the experimentally measured absolute maximum output error of 8.3, which corresponds to a displacement measurement error of 160 μm.

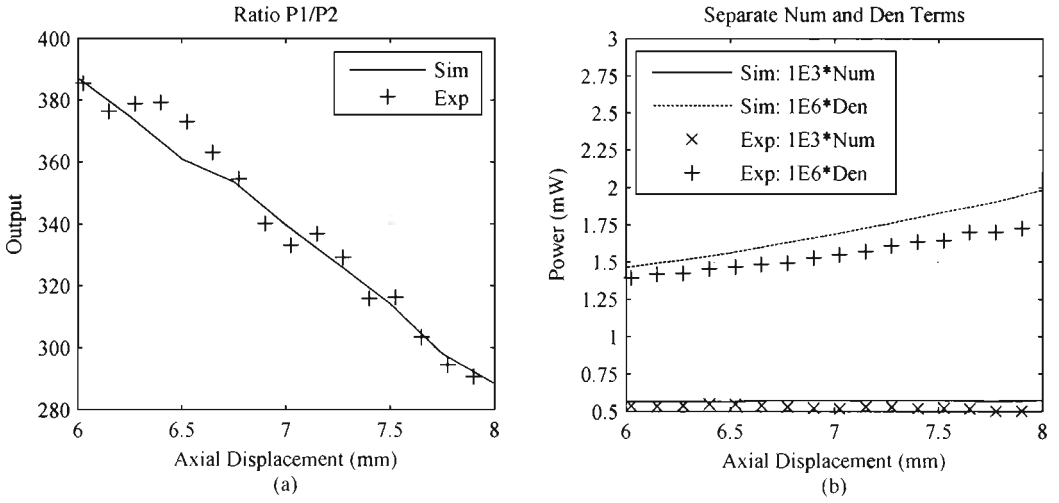

Figure 13. A comparison between experimental results and simulation results shows reasonable agreement.

Note in Figure 13 that both the experimentally measured numerator and denominator terms decrease relative to their simulated counterparts as the axial displacement increases. An advantage of the differential sensing approach is that sensor performance is not affected by this discrepancy, since it takes place in both the numerator and the denominator terms. As a result, the level of agreement between experimental sensor output and simulated sensor output does not diminish for large axial displacements. The robustness of the differential sensing approach was further evaluated by changing the source power level during testing (Figure 14). While decreasing the SLD output power from 3.99 mW to 2.77 mW the ratio P_1/P_2 remained nearly constant as a function of axial displacement. However, when the SLD output power was further decreased to 0.66 mW, the relationship between ratio P_1/P_2 and axial displacement changed notably. This loss of robustness is attributed to the fact that for low transmission power levels the term P_2 falls below the experimental noise floor, at which point it is no longer impacted by changes in source power level in the same way that the term P_1 is. In other words, for high source power levels changes in the source power level affect both the P_1 and P_2 similarly, resulting in robust performance, but for low transmission power levels these changes impact much less significantly any measurements that are at or below the noise floor. Since the differential sensing architecture is robust to environmental and hardware fluctuations, so long as the measured power levels P_1 and P_2 remain larger than the experimental noise floor, no calibration is required to operate this displacement sensor.

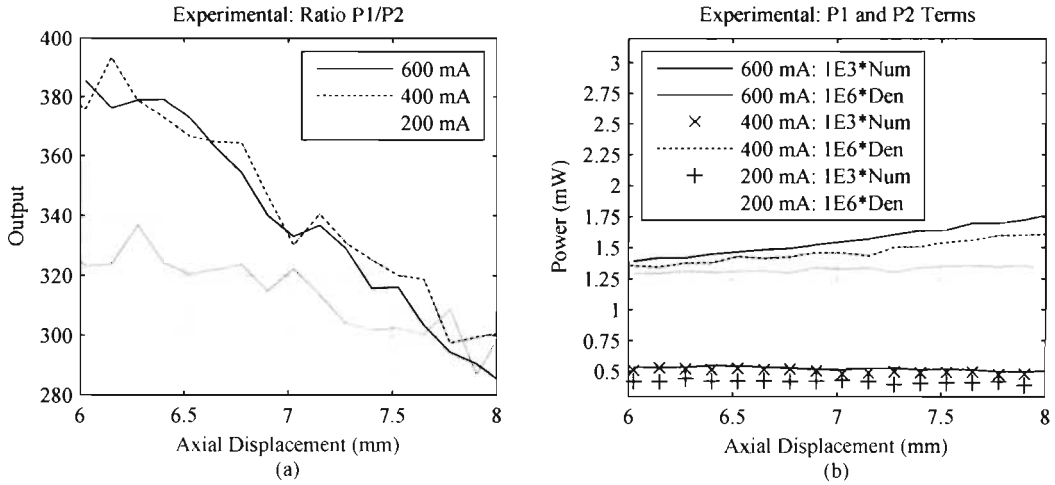

Figure 14. A change in the source power level from 3.99 mW to 2.77 mW does not significantly impact sensor performance. However, a further decrease in source power level to 0.66 mW does impact sensor performance.

Some uncertainty surrounds fiber locations in the bundle, although as discussed earlier in this section, the location of the single receiving fiber that is measured as P_2 is well-known, and any other variations in fiber location are expected to average over the receiving group that is measured as P_1. Therefore, uncertainty in receiving fiber locations is expected to have a negligible effect on sensor performance. There is also uncertainty present in the estimation of the loss mechanisms in the experimental setup. The effects of any losses prior to the transmission from the bundled assembly are negated by the differential sensing approach, but the sum total of loss mechanisms that occur after the signal emits through the transmitting fiber tip must be estimated. Unaddressed sources of uncertainty include the mechanical vibrations in the experimental setup, uncertainty and performance limitations of the micrometers that controlled the translation of the target surface, the initial calculation of displacement, uncertainty in the indices of refraction of the fiber core and cladding and in the optical properties of the rest of the components used in the bundled assembly. While it is impossible to conclude whether or not these sources of uncertainty entirely account for the discrepancies between simulation results and experimental results (Figure 14), the agreement is good enough that it is expected that they do.

8. PROPOSED CONTINUATIONS OF RESEARCH

As future work, I am proposing characterizing the sources of measurement and modeling uncertainty that resulted in disagreement between the optimization model results and the experimental performance of the optimized bundle. Following this analysis, I plan to use knowledge of the relationship between predicted results and actual results, and lessons learned from the first iteration, to propose a second iteration prototype bundle. The design of this second prototype will be dictated by a more in depth understanding of physical hardware limitations and the relationship between performance specifications and bundle architecture. The performance of this second iteration bundle may then be analyzed in terms of the optimization model uncertainty and the experimental uncertainty, with a thorough model validation and uncertainty analysis. The fundamental performance specifications of this second iteration bundle will then be evaluated in terms of their uncertainty, and in this way a framework for application-specific sensor design will be established. As presented in Section 1 the original proposed goal was to design a simple, non-contacting optical displacement sensor, with high-performance, and explain how this research path goes about achieving this goal in such a way as to achieve high combinations of performance metrics. The proposed steps will provide the basis for a sensor design approach that may be utilized in designing application specific intensity-modulated optical displacement sensors subject to a broad range of constraints, hardware selections, and performance limitations.

Future work will also include a thorough performance characterization of the EFPI displacement sensor in terms of the sources and degree of uncertainty. This will provide the basis for a design approach that may be generalized to meet application-specific sensor design needs. Further, when used in conjunction with the presented intensity-modulated displacement sensor design approach, this will enable a user to make a side-by-side comparison of the two sensing methodologies, with achievable performance calculated in terms of uncertainty.

REFERENCES

[1] Kersey, A. D. and Dandridge, A., "Applications of fiber-optic sensors," IEEE Transactions on Components, Hybrids, and Manuf. Technol. 13 (1), 137-143 (1990).

[2] Kersey, A. D., "A review of recent developments in fiber optic sensor technology," Optical Fiber Technol., 2, 291-317 (1996).

[3] Culshaw, B., "Optical fiber sensor technologies: Opportunities and – perhaps – pitfalls," J. of Lightwave Technol., 22 (1), 39-50 (2004).

[4] Murphy, K. A., Gunther, M. F., Vengsarkar, A. M., and Claus, R. O., "Quadrature phase-shifted, extrinsic Fabry-Perot optical fiber sensors," Opt. Lett., 16 (4), 273-275 (1991).

[5] Cabral, A. and Rebordao, J., "Accuracy of frequency-sweeping interferometry for absolute distance metrology," Optical Eng. 46 (7), 073602:1-10 (2007)

[6] Frank, W. E., "Detection and measurement device having a small flexible fiber transmission line," U.S. Patent 3,273,447 (Sep. 20, 1966).

[7] Kissinger, C. D., "Fiber optic proximity probe," U. S. Patent 3,327,584 (June 27, 1967).

[8] Cook, R. O. and Hamm, C. W., "Fiber optic lever displacement transducer," Appl. Opt., 18 (19), 3230-3241 (1979).

[9] Suganuma, F., Shimamoto, A., and Tanaka, K., "Development of a differential optical-fiber displacement sensor," Appl. Optics 38(7), 1103-1109 (1999).

[10] Li, X., Nakamura, K., and Ueha, S., "Reflectivity and illuminating power compensation for optical fibre vibrometer," Meas. Sci. Technol., 15, 1773-1778 (2004).

[11] Shimamoto, A. and Tanaka, K., "Geometrical analysis of an optical fiber bundle displacement sensor," Appl. Optics 35 (34), 6767-6774 (1996).

[12] Huang, H., and Tata, U., "Simulation, implementation, and analysis of an optical fiber bundle distance sensor single mode illumination," Appl. Opt., 47 (9), 1302-1309 (2008).

[13] http://www.mtiinstruments.com/products/fiberopticmeasurement.aspx

[14] http://www.philtec.com/$2010Products.pdf

[15] Moro, E. A., Todd, M. D., and Puckett, A. D., "Performance characterization of an intensity-modulated fiber optic displacement sensor," Accepted for publication in Proc. SPIE: 21st International Conference on Optical Fiber Sensors (2011).

[16] Buck, J. A., [Fundamentals of Optical Fibers], John Wiley & Sons, Inc., New York, 66-84 (1995).

[17] Trudel, V., and St-Amant, Y., "One- dimensional single-mode fiber-optic displacement sensors for submillimeter measurements," Appl. Opt., 48 (26), 4851-4857 (2009).

[18] Moro, E. A., Todd, M. D., and Puckett, A. D., "Experimental validation and uncertainty quantification of a single mode optical fiber transmission model," J. of Lightwave Technol., 29 (6), 856-863 (2011).

[19] Siegman, A. E., "Beam Perturbation and Diffraction" in [Lasers], University Science Books, Mill Valley, CA, 727-728 (1986).

[20] St-Amant, Y., Gariepy, D., and Rancourt, D., "Intrinsic properties of the optical coupling between axisymmetric Gaussian beams," Appl. Optics 43(30), 5691-5704 (2004).

[21] Trucano, T. G., Swiler, L. P., Igusa, T., Oberkampf, W. L., and Pilch, M., "Calibration, validation, and sensitivity analysis: What's what," Reliability Engineering and System Safety, 91, 1331-1357 (2006).

[22] Hemez, F. M. and Tippets, T. B., "Verification and validation of a composite model. Draft Report of the Los Alamos LDRD-DR "Damage Prognosis" Project, Los Alamos National Laboratory, Los Alamos, NM.

[23] Moro, E. A., Todd, M. D., Puckett, A. D., "Experimental verification of a model describing the intensity-distribution from a single mode optical fiber," Accepted for publication in Proc. SPIE (2011).

[24] Grahn, R., Karimi, H., Wilson, K., Moro, E., and Puckett, A., "Performance comparison of fiber optic tips in interferometric displacement measurements," Accepted for publication in Proc. 29th IMAC (2011).